

# Tracking the evolution of the morphology and stress distribution of SIS thermoplastic elastomers under tension using atomic force microscopy

Ling Gao<sup>a</sup>, Haonan Liu<sup>b</sup>, Xiaobin Liang<sup>b</sup>, Makiko Ito<sup>b</sup> and Ken Nakajima <sup>b</sup>

<sup>a</sup>College of Chemistry and Chemical Engineering, Huanggang Normal University, Huanggang, Hubei, China;

<sup>b</sup>Department of Chemical Science and Engineering, School of Materials and Chemical Technology, Tokyo Institute of Technology, Tokyo, Japan

## ABSTRACT

Styrene-based ABA-type triblock copolymers and their blends are widely investigated thermoplastic elastomers (TPEs). The design of tough TPE materials with high strength and resilience requires further clarification of the relationship between microstructure and macroscopic properties of stretched samples. Here, we applied atomic force microscopy (AFM)-based quantitative nanomechanical mapping to study the deformation behavior of poly(styrene-*b*-isoprene-*b*-styrene) blends under tension. The results indicated that the glassy polystyrene (PS) domains deformed and inhomogeneous stress distributions developed in the initial stretching stage. At 200% strain, the glassy PS domains started to crack. The change in the peak value in the JKR Young's modulus diagram during stretching was consistent with the stress – strain curve. Analysis of the particles before and after stretching suggested that the glassy domains separated and reorganized during stretching.

## ARTICLE HISTORY

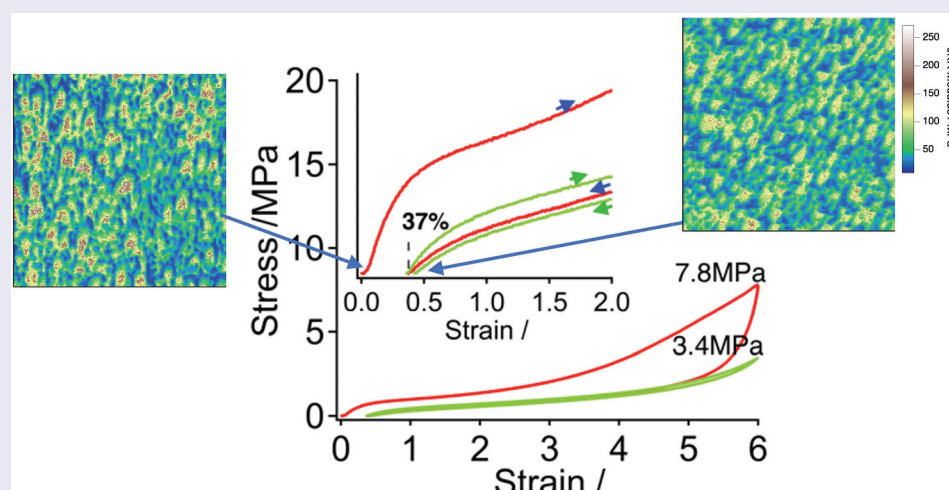
Received 30 July 2024

Accepted 5 September 2024

Revised 2 September 2024

## KEYWORDS

Thermoplastic elastomers; atomic force microscopy; quantitative nanomechanical mapping; deformation behavior; stress distribution





## IMPACT STATEMENT

A tough thermoplastic elastomer (TPE) with high strength and resilience was developed using styrene-based triblock copolymers and their blends, with its high-performance mechanism analyzed through AFM-based quantitative nanomechanical mapping.

## 1. Introduction

Thermoplastic elastomers (TPEs) have aroused increasing attention because they display elastic behavior at room temperature and processability comparable to that of thermoplastics at high temperatures [1–6]. Styrenic TPEs are extensively used due to their outstanding properties that rival those of conventional vulcanized (*i.e.*, chemically cross-linked) rubber [7]. Recently, many efforts have

been made to enhance the performance of TPEs through the design of molecular architectures, such as the introduction of miktoarms [8,9], transient cross-linking [10,11], multiblocks [12,13], and blending [14,15]. In particular, polymer blending is a convenient way to obtain desired nanoscale morphologies by varying component ratios and has been shown to affect macroscopic stress – strain response. This approach is preferable to the

**CONTACT** Ken Nakajima  [knakaji@mac.titech.ac.jp](mailto:knakaji@mac.titech.ac.jp)  Department of Chemical Science and Engineering, School of Materials and Chemical Technology, Tokyo Institute of Technology, Tokyo 152-8552, Japan

© 2024 The Author(s). Published by National Institute for Materials Science in partnership with Taylor & Francis Group.

This is an Open Access article distributed under the terms of the Creative Commons Attribution-NonCommercial License (<http://creativecommons.org/licenses/by-nc/4.0/>), which permits unrestricted non-commercial use, distribution, and reproduction in any medium, provided the original work is properly cited. The terms on which this article has been published allow the posting of the Accepted Manuscript in a repository by the author(s) or with their consent.

synthesis of new materials or the addition of other materials to improve compatibility. Nevertheless, it is difficult to obtain a comprehensive understanding of how the microstructure of these TPEs determines their macroscopic stress response under strain-induced deformation, and this has yet to be determined.

Styrene-isoprene-styrene (SIS) triblock copolymers have become common TPEs as their rigid polystyrene (PS) domains are dispersed in a rubbery polyisoprene (PI) matrix and serve as physical cross-links. Recently, some reports pointed out that the mechanical properties of block copolymers can be fine-tuned by introducing asymmetric, graft, and star-shaped structures [9]. Adhikari et al. used a fracture mechanics approach to investigate the toughness of block copolymer/PS blends and binary block copolymer blends, and their results identified a transition from brittle to tough behavior when the morphology changed from highly ordered lamellae to worm-like PS domains in a rubbery matrix [16,17]. Matsen used self-consistent field theory (SCFT) to investigate the phase behavior of asymmetric  $A_1BA_2$  triblock copolymer melts and observed a drastic shift in phase transition lines relative to those of symmetric ABA copolymers and asymmetric triblock copolymers [8]. From a practical point of view, styrene-based binary block copolymer mixtures with asymmetric styrene end blocks can substantially shift phase boundaries and achieve a balance of stiffness/toughness ratios over a wide composition range, resulting in enhanced toughness and processability of TPEs. To maintain the recoverable elasticity of a TPEs, its PS blocks usually assemble into a spherical or cylindrical morphology in the rubbery matrix; the volume fraction of PS ( $f_{PS}$ ) in commercial TPEs is generally below 0.3. Desirable asymmetric triblock copolymer blends with a high glassy PS fraction ( $f_{PS} > 0.3$ ) and spherical (or cylindrical) morphology yield tough TPEs with high strength and recoverable elasticity.

Recently, atomic force microscopy (AFM) has been developed as a facile way to visualize not only the morphology but also the micromechanical properties of materials [18–23]. Based on this technology, the interface morphology and nanomechanical properties of polymers such as amorphous [24], semicrystalline [25,26], particle-filled [27,28], rubber filler [29–31] and block copolymers [32] have been analyzed quantitatively. Since the micromechanical processes of deformation and fracture bridge the gap between morphology and mechanical properties, AFM technology is expected to provide insight into structure-property correlations and mechanisms of the nanomechanical deformation of block copolymer blends. In our recent work [33], we confirmed that PS domains in the microstructure of TPEs undergo deformation,

separation, and reorganization during stress-relaxation processes while elongated.

In this paper, we report observations of spherical morphologies in SIS/aSIS specimens prepared by blending symmetric SIS and asymmetric  $S_1IS_2$  samples. The relationship between the evolution of nanomechanical properties and macroscopic mechanical behavior under tension was the focus of our study. Our results for Young's modulus mapping and particle analysis before and after stretching suggested that the discontinuous glassy PS domains decomposed and reorganized during stretching. The 35% weight fraction of glassy PS and unevenly distributed spherical morphology apparently contributed to the toughness and ductility of the asymmetric SIS blends.

## 2. Experimental

### 2.1. Materials and sample preparation

Homo polystyrene (hPS,  $M_w = 19.2 \times 10^4$  g/mol), diblock polystyrene-*b*-polyisoprene (dSI, 75 wt.% PS,  $M_w = 43.6 \times 10^4$  g/mol), symmetric SIS (SIS, 22 wt.% PS,  $M_w = 11 \times 10^4$  g/mol), symmetric SIS (sSIS, 44 wt.% PS,  $M_w = 8.7 \times 10^4$  g/mol) and asymmetric  $S_1IS_2$  (aSIS, 69 wt.% PS,  $M_w = 36 \times 10^4$  g/mol,  $M_{PS, long} = 23 \times 10^4$  g/mol) were provided by the Zeon Corporation and used in this study for preparing blends, the schematic diagram of pure polymer sample composition was shown in Figure 1(a). SIS was blended with hPS, dSI, sSIS, and aSIS through the melting process to prepare an SIS-blend with 35 wt.% PS content, the schematic diagram of blend composition shows in Figure 1(b). The details of the blend compositions of polymers are summarized in Table 1. The mixed materials were added into a twin-screw microcompounder for extrusion at 230°C at 100 rpm for 5 min under nitrogen. The extrudates were sequentially hot-pressed three times at 170°C under 20 MPa for 20 s to prepare 1 mm thick films.

### 2.2. Nanomechanical property measurement

The films were cut using a Leica EM FC6 ultramicrotome (Leica Microsystems, Germany) at  $-120^\circ\text{C}$  to obtain flat surfaces for AFM characterization. The AFM measurements were made using the PeakForce quantitative nanomechanics mode with a commercial AFM system (Multimode 8 with a Nanoscope V controller, Bruker AXS, USA) under ambient conditions. Force – deformation curves were collected over randomly selected surfaces at a scale of approximately  $1 \mu\text{m} \times 1 \mu\text{m}$  and a resolution of  $256 \times 256$  pixels using a silicon cantilever (tip radius:  $2 \sim 8$  nm; spring constant:  $0.50 \sim 1.8$  N/m; resonance frequency:  $\sim 70$  kHz). The actual spring constant was measured by the

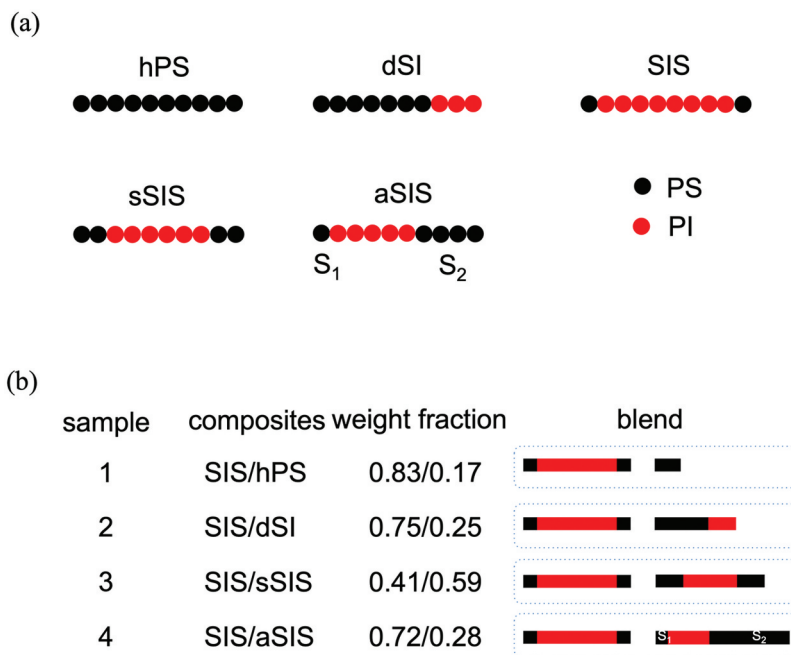


Figure 1. (a) Schematic diagram of pure polymer sample composition. (b) Schematic diagram of blend sample composition.

Table 1. Molecular characteristics of SIS blends.

Sample no.	composites	character	Weight fraction of PS ( $w_{PS}$ )	Weight fractions	$M/10^3$
0	Neat SIS	symmetric	22%	100/0	110
1	SIS/hPS	blend	35%	83/17	123
2	SIS/dSI	blend	35%	75/25	188
3	SIS/sSIS	blend	35%	41/59	96
4	SIS/aSIS	blend	35%	72/28	180

thermal tuning method. The radius of the probe was evaluated by scanning the TipCheck sample (Bruker AXS, USA) in QNM mode with a scan rate, scan size, and image resolution of 0.5 Hz,  $2 \mu\text{m} \times 2 \mu\text{m}$ , and  $1024 \times 1024$  pixels, respectively. As described in our previous papers [32,34], Johnson-Kendall-Roberts (JKR) contact mechanics are suitable to accurately reproduce the force – deformation curves on the surfaces of soft materials. According to the above model, the local JKR elastic modulus  $E$  (hereafter JKR modulus) is expressed as:

$$E = -\frac{3(1 - \nu^2)}{4} \frac{1.27F_1}{\sqrt{R(\delta_0 - \delta_1)^3}} \quad (1)$$

where  $\nu$  is Poisson’s ratio and  $R$  is the radius of the curvature of the tip.  $\delta_0$  and  $\delta_1$  are the indentation depths when the adhesive and elastic restoring forces are equivalent, and the adhesive force is maximum ( $F_1$ ). A two-dimensional map of the JKR modulus based on the JKR analysis was also obtained.

For comparison, tensile tests were performed using a Shimadzu EZ-S tensile tester (Shimadzu Corporation, Japan) at room temperature ( $\sim 25 \text{ }^\circ\text{C}$ ). Specimens with a thickness of  $\sim 1 \text{ mm}$  were cut with a dumbbell shape (size,  $20 \text{ mm} \times 2 \text{ mm}$ ). The specimens were uniaxially

stretched at a crosshead speed of  $40 \text{ mm/min}$ . Three or more replicate specimens were tested to obtain a good set of statistics for the measured values.

### 3. Results and discussion

#### 3.1. Four types of binary block copolymer blends containing 35 wt.% styrene

By blending different polymers with SIS, four block copolymer blends with the same styrene content were obtained. As shown in Figure 2(a), although the styrene content is the same, the stress – strain curves are completely different. The deformation behavior of the blends shows different ductility and toughness. A cold drawing phenomenon is observed in the SIS/sSIS blend system in which a macroscopic necking zone forms after high yield strength, and finally, the specimen undergoes a plastic-to-rubber transition at very high strains. However, typical TPE deformation behavior is observed in the blended samples of SIS/hPS, SIS/dSI, and SIS/aSIS. Among them, SIS/aSIS shows higher strength of  $15 \text{ MPa}$  and elongation up to  $800\text{--}900\%$ . This is a direct indication that the mechanical behaviors of blends are strongly affected by the nature

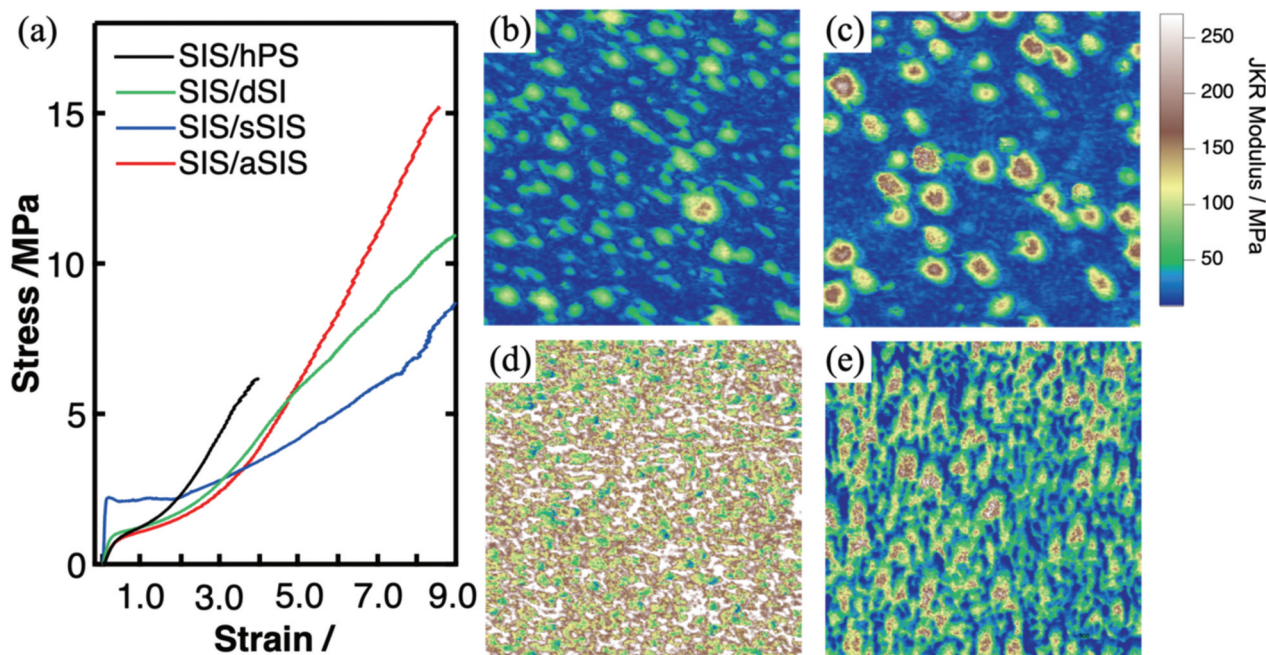


**Figure 2.** (a) Stress-strain curves of four sis-blends and JKR modulus maps of (b) SIS/hPS, (c) SIS/dSI, (d) SIS/sSIS and (e) SIS/aSIS. The scan size is 1.0  $\mu\text{m}$ .

of the microphase-separated morphology in addition to the chemical composition.

In the JKR modulus maps (Figure 2(b–e)), the high modulus areas correspond to the glassy PS domain, while the low modulus areas correspond to the PI domain. SIS/sSIS shows a relatively high JKR modulus, which is consistent with the data obtained from the macroscopic stress – strain curve. In the SIS/sSIS blend, as shown in Figure 2(d), the PS disperses in the PI matrix to form a network structure. An explanation has been reported [16] for the macroscopic necking that occurs in symmetric triblock copolymers where, above the yield point, the applied stress is high enough to cause considerable orientation of the PS chains and collapse of the rigid PS domain. However, due to the complexity of symmetric SIS blends, the structure-effect relationships between their microstructure and macroscopic properties are still unclear and need to be further discussed. In the other three blend samples, similar spherical-like PS phases embedded in rubbery PI domains are observed. These three blends show similar macroscopic tensile behavior at the initial strain (<1). At the beginning of stretching, the strain is mainly in the soft matrix, and the rubber chains orient along the stretch direction. The asymmetric SIS mixture shows higher ductility and strength. Both ends of the rubbery PI blocks present in the SIS/aSIS blends are immobilized by the PS phase, forming strong physical cross-linking sites and thus enhancing the mechanical properties of the blended samples. In contrast, for SIS/hPS or SIS/dSI blends, homo PS or dSI only dangles in the PS domains without bridging them, resulting in many fewer physical crosslinking sites than in SIS/aSIS.

### 3.2. Morphology and nanomechanical properties of SIS/aSIS

Before discussing blends, it is essential to evaluate the mechanical properties and nanostructure of neat block copolymers. Neat symmetric SIS ( $w_{\text{PS}} = 22$  wt.%) has strong elastic deformation and a tensile strength of 8 MPa at 1000% strain due to a large number of rubber PI phases. The asymmetric aSIS stress – strain curve has a yield stress of 17 MPa with a post-yield hardening curve that breaks at a stress of 21 MPa (Figure 3(a)). In contrast, the stress – strain curve of the blended SIS/aSIS sample exhibits a highly non-linear stress – strain response of a typical TPE, with high tensile strength up to 15 MPa and strain up to 1000%.

Microphase-separated morphologies consisting of bright (glassy PS phase) and dark (rubbery PI phase) domains are observed in neat SIS and aSIS specimens, as shown in the AFM original height images (Figure 3(b,c)). Since limited mobility prevents the molecules from reaching equilibrium during the melting process, it is difficult for them to form a self-assembled structure with long-range order. Nevertheless, cylinder-like and lamellar morphologies with periodicities of 30 and 65 nm were observed in SIS and aSIS, respectively. A completely different microscopic phase separation structure is observed in SIS/aSIS, as shown in Figure 3(d–f). According to the JKR modulus map and adhesion force map of SIS/aSIS with 35 wt.% PS, the blue area in the JKR modulus map corresponding to the yellow – red area with low

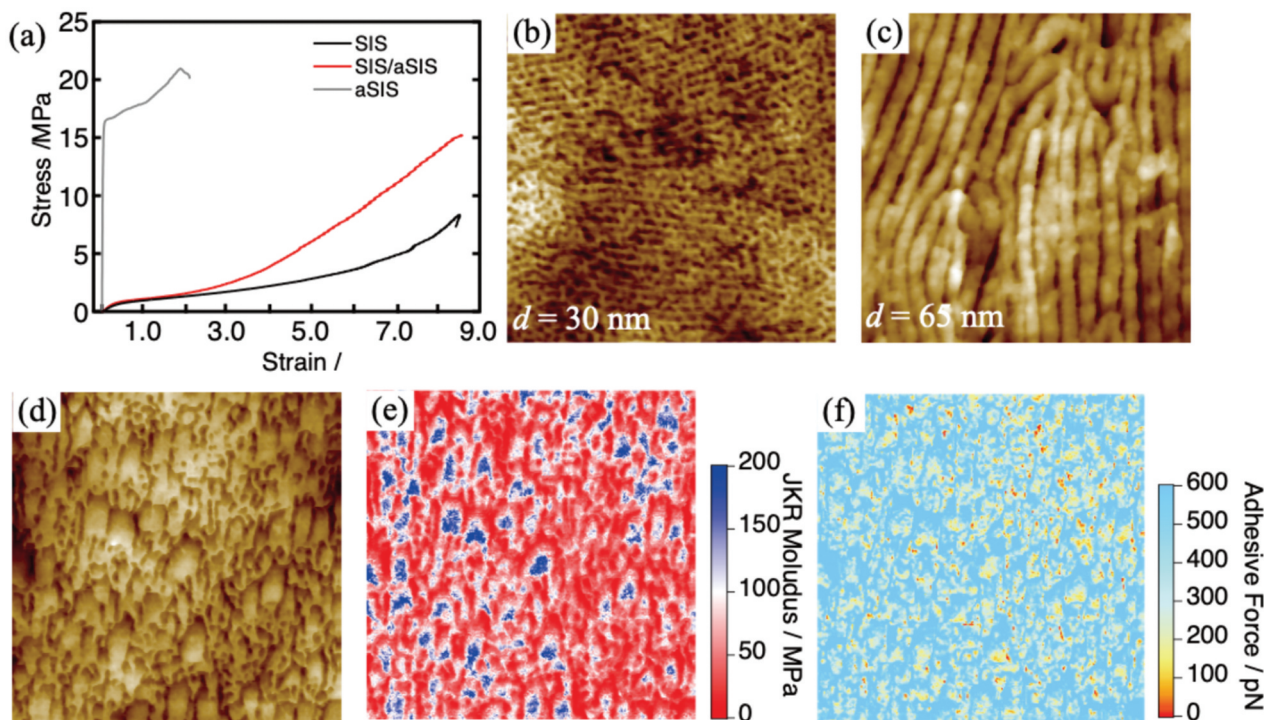


**Figure 3.** (a) Stress-strain curves, AFM height images of (b) symmetric SIS ( $w_{PS} = 22 \text{ wt.}\%$ ), (c) asymmetric SIS ( $w_{PS} = 69 \text{ wt.}\%$ ), and (d) height image, (e) JKR modulus map, and (f) adhesive force map of SIS/aSIS ( $w_{PS} = 35 \text{ wt.}\%$ ). The scan size is  $1.0 \mu\text{m}$ . It should be noted that the stress-strain curves of SIS/aSIS here are the same as those of SIS/aSIS in Figure 2(a).

adhesion belongs to the hard PS phase, while the red area in the JKR modulus map corresponding to the light blue area with high adhesion belongs to the PI domain. Unexpectedly, discontinuous PS phases with various particle sizes were embedded in the rubber PI matrix by blending cylindrical SIS and lamellar aSIS. The presence of the asymmetric PS block apparently enables selective phase separation of PS with different molecular weights to form PS domains with various particle sizes, as shown in Figure 3(e,f). The different morphologies of the three samples might temporarily give them very different stress – strain responses, especially for SIS and SIS/aSIS. In the early stages of stretching (less than approximately 200%), the easily deformable soft PI matrix stretches; thus, SIS and SIS/aSIS have similar responses with gradually increasing stress. As elongation continues, the deformation of the soft PI matrix reaches its limit, and the hard PS domain of different particle sizes in SIS/aSIS withstands greater stress without damage compared to that in SIS, thus producing a unique self-reinforcement phenomenon at the later stage. In addition, some studies have shown that block copolymers with asymmetric structures are more likely to form phase-separated structures of bridge chains due to differences in surface entropy, which also results in better strength [35].

### 3.3. Nanomechanical properties and stress-strain curves

Microscopic deformation and micromechanical behavior during the stretching process were observed to obtain evidence of the relationship between asymmetric molecular structure and macroscopic mechanical properties. We used a new method based on AFM nanomechanics to visualize the evolution of the morphology and JKR modulus under strain-induced deformation as a specimen was stretched from 0% to 200% strain [36]. As shown in Figure 4, the red area corresponds to the PI domain with a low modulus, and the blue area corresponds to the PS domain with a high modulus. The double-headed arrows represent the stretching direction. The right side of the figure is the corresponding histogram of the distribution of the JKR modulus. The deformation behavior and the evolution of the stress distribution at the nanometer scale are directly observed. As the strain increases, the glassy PS domain deforms from spherical to prolate spheroid, and the stress distribution of the sample moves in the direction of high modulus. When the sample is stretched to 50%, connections are observed in the high modulus region as shown in Figure 4(b), and shoulder peaks appear near 120 MPa. The distance between the PS domains in the stretch direction increases when stretched, and the PS field in the depth direction is, therefore, close to the surface. These results confirm an inhomogeneous stress distribution

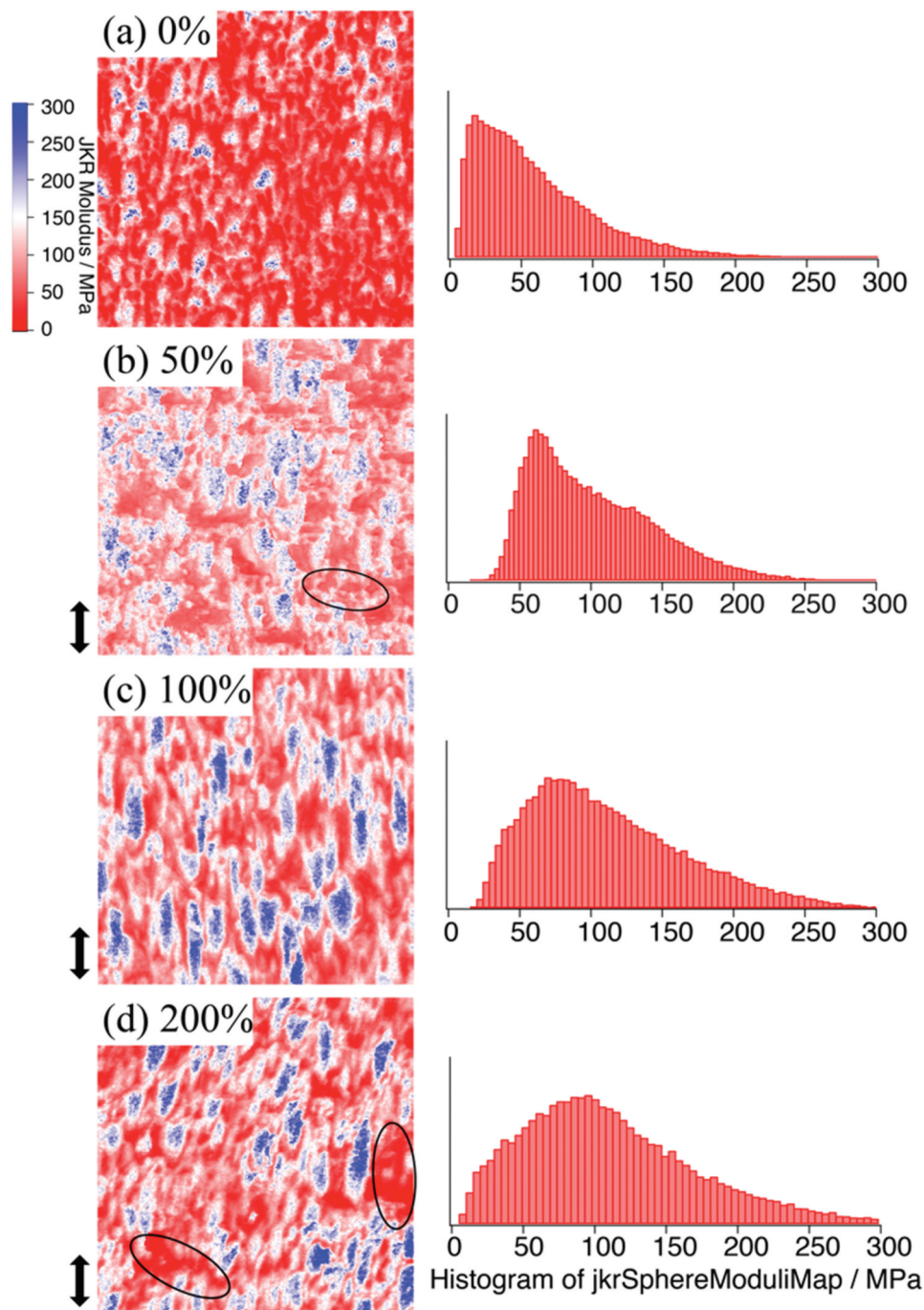


**Figure 4.** JKR modulus maps of SIS/aSIS sample with the strain of (a) 0%, (b) 50%, (c) 100%, (d) 200% and the histogram distribution of JKR modulus, respectively. The scan size is 1.0  $\mu\text{m}$ . Cavitation might occur in the region identified with ellipses in (d).

and the formation of stress chains due to stress concentrations. As the strain-induced deformation increases, the shoulder peaks in the vicinity of 100 MPa disappear, and the stress distribution tends to polarize. At 200% strain, the prolate spheroid glassy PS domain becomes short, and cavitation appears in some areas (the elliptical regions in Figure 4(d)). This may be a result of the onset of breakup of glassy PS during stretching. At the initial deformation stage, elastic deformation predominates, and the orientation of the PS phases is rather weak. At 200% strain, the local stress increases, the glassy PS phase stretches, and

cavitation may occur first in the larger PS domain to form cracks.

The microscopic JKR modulus of hard and soft phases under different strains was also analyzed for comparison with macroscopic mechanical data. Since the PS and PI phases have different adhesive features, in Figure 5(a), the JKR modulus distribution of SIS/aSIS can be further divided into two areas by the binary adhesive force map. In Figure 5(b), the stress – strain curve (red line) refers to the left Y-axis (left arrow), and the micro-modulus under different strains refers to the JKR modulus on the right Y-axis (right

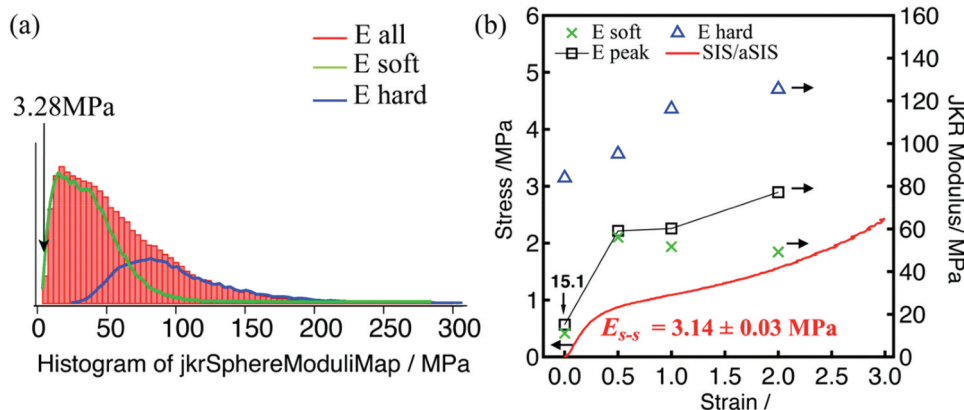


**Figure 5.** (a) The complete histogram of JKR modulus distribution of SIS/aSIS sample before stretching with the hard (blue line) and soft (green line) domain distribution. (The scan size is 1  $\mu\text{m}$ .) and (b) comparison chart of tensile strength and nanomechanical properties. In (b), the stress curve corresponds to the left Y-axis (red curve, leftward arrow) and JKR modulus corresponds to the right Y-axis (black curve, blue dot, and green X's, rightward arrow).

arrow), including the peak values of the hard-domain modulus (blue dots), soft-matrix modulus (green dots), and entire map (black curve). Notably, the peak of the JKR modulus without stretching ( $\sim 15$  MPa), which is normally regarded as a microscopic Young's modulus, is higher than the macroscopic Young's modulus ( $\sim 3.14$  MPa) obtained from the stress – strain curve. It should be taken into account that the small scanning area for AFM is not comparable to the entire sample. In addition, the effect of the adjacent hard domain during soft-matrix deformation cannot be eliminated, overestimating the modulus of the soft matrix. In the JKR modulus histogram, although the minimum modulus of the soft phase is approximately 3.28 MPa, which is similar to the JKR modulus obtained from the stress – strain curve, it is still difficult to determine the relationship between them. The JKR modulus image shows that as the strain increases, the total modulus  $E$  also increases due to the stress distribution, which has been confirmed in our previous study. Interestingly, the JKR modulus of the PI phase decreases even if the total modulus increases, which can be interpreted as the full extension of the rubbery phase during the stretching process and the

relief of stress concentration. The stress tends to concentrate in the glassy PS phase, which deforms or even splits the PS phase, leading to stress relaxation in the PI phase and showing a decrease in the JKR modulus of PI with stretching. Notably, the structural changes caused by the separation of the PS phase have a permanent effect on the material with residual strain, which we analyze in detail in the next section. Although the micro-modulus cannot be directly compared with the macro-stress value, the peak change diagram of the JKR modulus is consistent with the stress – strain curve. Undoubtedly, AFM technology can be used to directly observe structural deformation and help understand the relationship between structure and performance.

### 3.4. Comparing the microscopic structure and properties before and after deformation

To gain better insight into the microscopic mechanisms of residual strain, we investigated the hysteresis behavior of SIS/aSIS after deformation and the changes in microstructure and properties after removal of external stresses. In Figure 6(a), we present the hysteresis curves

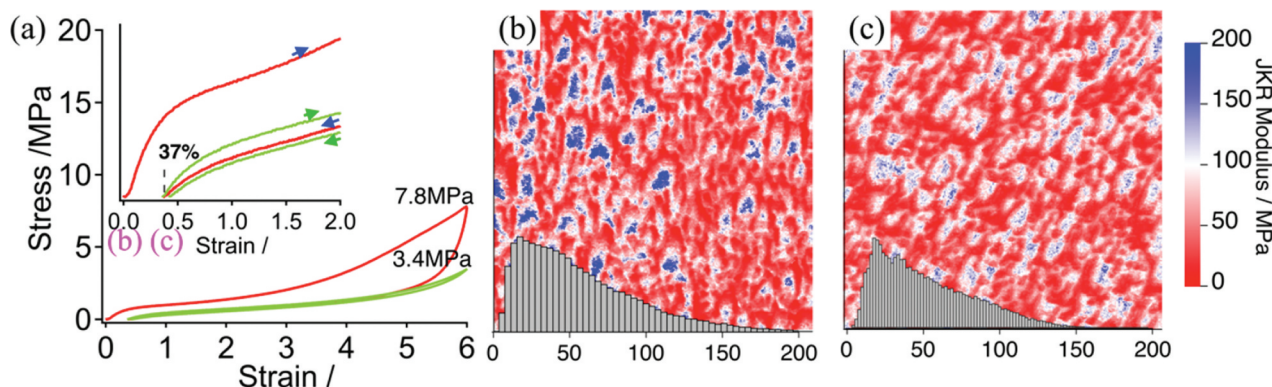


**Figure 6.** (a) Hysteresis curves for the SIS/aSIS sample during two cycles to 600% strain at 40  $\text{mm min}^{-1}$ . JKR modulus maps and distributions for the SIS/aSIS sample (b) before stretching and (c) after a hysteresis cycle to 600% strain. The scan size is 1.0  $\mu\text{m}$ .

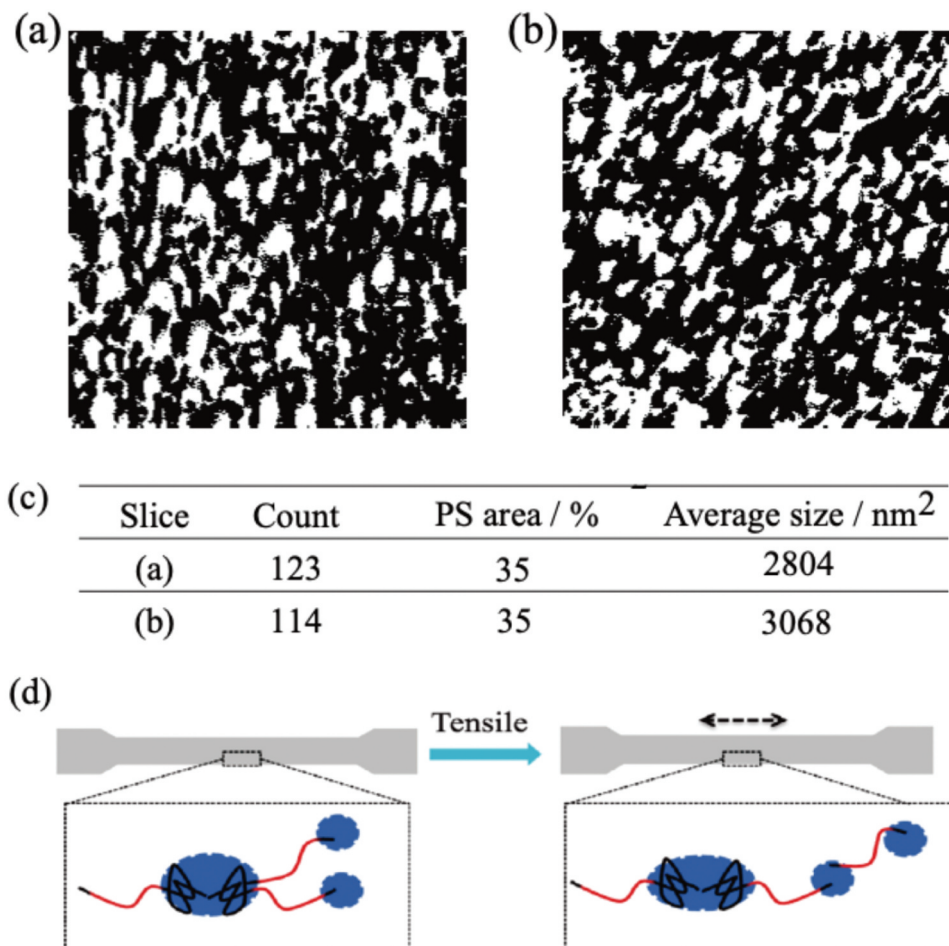


**Figure 7.** Binary images of the SIS/aSIS sample (a) before stretching and (b) after a hysteresis cycle of 600% strain. The scan size is 1.0  $\mu\text{m}$ . (c) Particle analysis data obtained from ImageJ. (d) Reorganization mechanism of PS phases during tensile strain.

for two cycles to 600% strain at 40 mm/min. The results show that the samples have 37% residual strain after the first tensile cycle and that the stress decreases at 600% strain in the second stretch, but there is little change in residual strain and stress after two cycles of loading. We also observe a decrease in the microscopic modulus of the samples after stretching in the JKR modulus image (Figure 6(b,c)). This result may be caused by the plastic deformation of certain microstructures during the first hysteresis loop, accompanied by a slight loss of recoverable elasticity. To elucidate the microscopic mechanism, we made binary versions of the JKR modulus images and analyzed them, as shown in Figure 7(a,b). Irregular spherical phase separation structures are observed in the two SIS samples before and after tension, where the white area corresponds to the hard PS phase, and the black area belongs to the soft PI phase. The images obtained by particle analysis show that there is a change from the original hard PS particles with different sizes particles that are more uniform in size after deformation. This can be considered a result of splitting of the large PS phase after receiving a stress concentration. For image analysis, ImageJ was used to convert the binary images into digital images of  $256 \times 256$  pixels and then analyze the particles. The image parameter of the

size is set from 0 to infinity, and the circularity is from 0.03 to 1.00 to calculate the shape of the discontinuous hard domain. Interestingly, the analytical results shown in Figure 7(c) show a decrease in the number of PS phases and a slight increase in the average particle size, which indicates that some of the particles reorganized. We can speculate that in relatively short PS, molecules are more likely to be pulled out of large glassy PS phases under external forces, and they more readily reorganize with other PS phases, the schematic diagram of which is shown in Figure 7(d). This is consistent with the results described in other studies of glass domain deformation before and after micro stress concentration [37,38]. The splitting and recombination of the PS phase at the nanometer scale can explain the strength and toughness of the asymmetric mixture. In future work, the strength and ductility of TPE materials with worm-like or cylindrical structures in asymmetric systems will be further studied.

## 5. Conclusions

The mechanical behaviors of triblock copolymer blends are dramatically affected by the nature of their micro-phase-separated morphology. A special phase



separation structure with PS phases of different particle sizes formed in an SIS/aSIS blend and made the blend elastic despite a high PS content. In addition, AFM-based quantitative nanomechanical mapping was applied to track the evolution of the morphology and stress distribution of an SIS/aSIS blend during stretching. A mesh-like continuous phase and shoulder peaks near 100 MPa at 50% strain were observed, confirming the presence of stress concentrations and an inhomogeneous stress distribution. As the strain increased to 100%, the glassy PS domain deformed from spherical to oblate, and the stress distribution tended to become more homogeneous. At 200% strain, the prolate spheroid glassy PS domain became short, and cavitation occurred in some areas. Based on the analysis of the nano-stress distribution, we found that the splitting of the glassy PS phase led to the relaxation of stress in the PI phase and macroscopic residual strain. These microscopic findings provide theoretical support for the future development of tough TPE materials with high strength and recoverable elasticity.

## Disclosure statement

No potential conflict of interest was reported by the author(s).

## Funding

This work was supported by the Japan Science and Technology Agency (JST) Core Research for Evolutional Science and Technology (CREST) Grant Number JPMJCR17J4.

## ORCID

Ken Nakajima  <http://orcid.org/0000-0001-7495-0445>

## References

- [1] Holden G. Thermoplastic elastomers. In: Morton M, editor. Rubber technology. New York (NY): Springer; 1987. p. 465–481. doi: [10.1007/978-1-4615-7823-9\\_16](https://doi.org/10.1007/978-1-4615-7823-9_16)
- [2] Watts A, NKurokawa N, Hillmyer MA. Strong, resilient, and sustainable aliphatic polyester thermoplastic elastomers. *Biomacromolecules*. 2017;18(6):1845–1854. doi: [10.1021/acs.biomac.7b00283](https://doi.org/10.1021/acs.biomac.7b00283)
- [3] McMullin E, Rebar HT, Mather PT. Biodegradable thermoplastic elastomers incorporating POSS: synthesis, microstructure, and mechanical properties. *Macromolecules*. 2016;49(10):3769–3779. doi: [10.1021/acs.macromol.6b00470](https://doi.org/10.1021/acs.macromol.6b00470)
- [4] Cho H, Mayer S, Pösel E, et al. Deformation mechanisms of thermoplastic elastomers: stress-strain behavior and constitutive modeling. *Polymer (Guildf)*. 2017;128:87–99. doi: [10.1016/j.polymer.2017.08.065](https://doi.org/10.1016/j.polymer.2017.08.065)
- [5] Schimpf V, Max JB, Stolz B, et al. Semicrystalline non-isocyanate polyhydroxyurethanes as thermoplastics and thermoplastic elastomers and their use in 3D printing by fused filament fabrication. *Macromolecules*. 2019;52(1):320–331. doi: [10.1021/acs.macromol.8b01908](https://doi.org/10.1021/acs.macromol.8b01908)
- [6] Yan J, Spontak RJ. Toughening poly(lactic acid) with thermoplastic elastomers modified by thiol-ene click chemistry. *ACS Sustain Chem Eng*. 2019;7(12):10830–10839. doi: [10.1021/acssuschemeng.9b01657](https://doi.org/10.1021/acssuschemeng.9b01657)
- [7] Indukuri KK, Lesser AJ. Comparative deformational characteristics of poly(styrene-*b*-ethylene-co-butylene-*b*-styrene) thermoplastic elastomers and cross-linked natural rubber. *Polymer (Guildf)*. 2005;46(18):7218–7229. doi: [10.1016/j.polymer.2005.06.025](https://doi.org/10.1016/j.polymer.2005.06.025)
- [8] Spencer RKW, Matsen MW. Domain bridging in thermoplastic elastomers of star block copolymer. *Macromolecules*. 2017;50(4):1681–1687. doi: [10.1021/acs.macromol.7b00078](https://doi.org/10.1021/acs.macromol.7b00078)
- [9] Shi W, Lynd NA, Montarnal D, et al. Toward strong thermoplastic elastomers with asymmetric miktoarm block copolymer architectures. *Macromolecules*. 2014;47(6):2037–2043. doi: [10.1021/ma402566g](https://doi.org/10.1021/ma402566g)
- [10] Hayashi M, Matsushima S, Noro A, et al. Mechanical property enhancement of ABA block copolymer-based elastomers by incorporating transient cross-links into soft middle block. *Macromolecules*. 2015;48(2):421–431. doi: [10.1021/ma502239w](https://doi.org/10.1021/ma502239w)
- [11] Ocano C, Fernández R, Tercjak A, et al. Nanostructured thermoplastic elastomers based on SBS triblock copolymer stiffening with low contents of epoxy system. Morphological behavior and mechanical properties. *Macromolecules*. 2013;46(9):3444–3451. doi: [10.1021/ma400152g](https://doi.org/10.1021/ma400152g)
- [12] Wang W, Lu W, Goodwin A, et al. Recent advances in thermoplastic elastomers from living polymerizations: macromolecular architectures and supramolecular chemistry. *Prog Polym Sci*. 2019;95:1–31. doi: [10.1016/j.progpolymsci.2019.04.002](https://doi.org/10.1016/j.progpolymsci.2019.04.002)
- [13] Zhang Q, Hua W, Ren Q, et al. Regulation of physical networks and mechanical properties of triblock thermoplastic elastomer through introduction of mid-block similar crystalline polymer with multiblock architecture. *Macromolecules*. 2016;49(19):7379–7386. doi: [10.1021/acs.macromol.6b01441](https://doi.org/10.1021/acs.macromol.6b01441)
- [14] Shi W, Li W, Delaney KT, et al. Morphology re-entry in asymmetric PS-PI-PS' triblock copolymer and PS homopolymer blends. *J Polym Sci Part B Polym Phys*. 2016;54(2):169–179. doi: [10.1002/polb.23811](https://doi.org/10.1002/polb.23811)
- [15] Shi W, Hamilton AL, Delaney KT, et al. Aperiodic “bricks and mortar” mesophase: a new equilibrium state of soft matter and application as a stiff thermoplastic elastomer. *Macromolecules*. 2015;48(15):5378–5384. doi: [10.1021/acs.macromol.5b01210](https://doi.org/10.1021/acs.macromol.5b01210)
- [16] Adhikari R, Michler RH. Influence of molecular architecture on morphology and micromechanical behavior of styrene/butadiene block copolymer systems. *Prog Polym Sci*. 2004;29(9):949–986. doi: [10.1016/j.progpolymsci.2004.06.002](https://doi.org/10.1016/j.progpolymsci.2004.06.002)
- [17] Adhikari R, Michler GH, Huy TA, et al. Correlation between molecular architecture, morphology, and deformation behaviour of styrene/butadiene block copolymers. *Macromol Chem Phys*. 2003;204(3):488–499. doi: [10.1002/macp.200390022](https://doi.org/10.1002/macp.200390022)
- [18] Wang D, Russell TP. Advances in atomic force microscopy for probing polymer structure and properties. *Macromolecules*. 2018;51(1):3–24. doi: [10.1021/acs.macromol.7b01459](https://doi.org/10.1021/acs.macromol.7b01459)
- [19] Zhang S, Liu H, Gou J, et al. Quantitative nanomechanical mapping on poly(lactic acid)/poly( $\epsilon$ -caprolactone)

- /carbon nanotubes bionanocomposites using atomic force microscopy. *Polym Test*. 2019;77:105904. doi: [10.1016/j.polymertesting.2019.105904](https://doi.org/10.1016/j.polymertesting.2019.105904)
- [20] Fujinami S, Ueda E, Nakajima K, et al. Analytical methods to derive the elastic modulus of soft and adhesive materials from atomic force microscopy force measurements. *J Polym Sci Part B Polym Phys*. 2019;57(18):1279–1286. doi: [10.1002/polb.24871](https://doi.org/10.1002/polb.24871)
- [21] Nishi T, Nukaga H, Fujinami S, et al. Nanomechanical mapping of carbon black reinforced natural rubber by atomic force microscopy. *Chin J Polym Sci*. 2007;25(1):35–41. doi: [10.1142/S0256767907001820](https://doi.org/10.1142/S0256767907001820)
- [22] Nakajima K, Ito M, Wang D, et al. Nano-palpatation AFM and its quantitative mechanical property mapping. *Microscopy*. 2014;63(3):193–208. doi: [10.1093/jmicro/dfu009](https://doi.org/10.1093/jmicro/dfu009)
- [23] Nakajima K, Watabe H, Nishi T. Single polymer chain rubber elasticity investigated by atomic force microscopy. *Polymer (Guildf)*. 2006;47(7):2505–2510. doi: [10.1016/j.polymer.2005.12.092](https://doi.org/10.1016/j.polymer.2005.12.092)
- [24] Liu H, Liu W, Fujie T, et al. Contact-induced stiffening in ultrathin amorphous polystyrene films. *Polymer (Guildf)*. 2018;153:521–528. doi: [10.1016/j.polymer.2018.08.050](https://doi.org/10.1016/j.polymer.2018.08.050)
- [25] Thomas C, Seguela R, Detrez F, et al. Plastic deformation of spherulitic semi-crystalline polymers: an in situ AFM study of polybutene under tensile drawing. *Polymer (Guildf)*. 2009;50(15):3714–3723. doi: [10.1016/j.polymer.2009.06.023](https://doi.org/10.1016/j.polymer.2009.06.023)
- [26] Wu X, Shi S, Yu Z, et al. AFM nanomechanical mapping and nanothermal analysis reveal enhanced crystallization at the surface of a semicrystalline polymer. *Polymer (Guildf)*. 2018;146:188–195. doi: [10.1016/j.polymer.2018.05.043](https://doi.org/10.1016/j.polymer.2018.05.043)
- [27] Kummali MM, Miccio LA, Schwartz GA, et al. Local mechanical and dielectric behavior of the interacting polymer layer in silica nano-particles filled SBR by means of AFM-based methods. *Polymer (Guildf)*. 2013;54(18):4980–4986. doi: [10.1016/j.polymer.2013.07.032](https://doi.org/10.1016/j.polymer.2013.07.032)
- [28] Jones R, Pollock HM, Geldart D, et al. Frictional forces between cohesive powder particles studied by AFM. *Ultramicroscopy*. 2004;100(1–2):59–78. doi: [10.1016/j.ultramic.2004.01.009](https://doi.org/10.1016/j.ultramic.2004.01.009)
- [29] Tian C, Chu G, Feng Y, et al. Quantitatively identify and understand the interphase of SiO<sub>2</sub>/rubber nanocomposites by using nanomechanical mapping technique of AFM. *Compos Sci Technol*. 2019;170:1–6. doi: [10.1016/j.compscitech.2018.11.020](https://doi.org/10.1016/j.compscitech.2018.11.020)
- [30] Nakajima K, Ito M, Nguyen HK, et al. Nanomechanics of the rubber–filler interface. *Rubber Chem Technol*. 2017;90(2):272–284. doi: [10.5254/rct.17.82642](https://doi.org/10.5254/rct.17.82642)
- [31] Lim YJ, Carolan D, Taylor AC. Simultaneously tough and conductive rubber–graphene–epoxy nanocomposites. *J Mater Sci*. 2016;51(18):8631–8644. doi: [10.1007/s10853-016-0122-2](https://doi.org/10.1007/s10853-016-0122-2)
- [32] Wang D, Nakajima K, Fujinami S, et al. Characterization of morphology and mechanical properties of block copolymers using atomic force microscopy: effects of processing conditions. *Polymer (Guildf)*. 2012;53(9):1960–1965. doi: [10.1016/j.polymer.2012.02.046](https://doi.org/10.1016/j.polymer.2012.02.046)
- [33] Liu H, Liang X, Nakajima K. Direct visualization of a strain-induced dynamic stress network in a SEBS thermoplastic elastomer with in situ AFM nanomechanics. *Jpn J Appl Phys*. 2020;59:SN1013. doi: [10.35848/1347-4065/ab948a](https://doi.org/10.35848/1347-4065/ab948a)
- [34] Liu H, Liang X, Nakajima K. Nanoscale strain–stress mapping for a thermoplastic elastomer revealed using a combination of in situ atomic force microscopy nanomechanics and Delaunay triangulation. *J Poly Sci*. 2022;60(22):3143–3140. doi: [10.1002/pol.20220345](https://doi.org/10.1002/pol.20220345)
- [35] Shi W, Lynd N, Montarnal D, et al. Toward strong thermoplastic elastomers with asymmetric miktoarm block copolymer architectures. *Macromolecules*. 2014;47(6):2037–2043. doi: [10.1021/ma402566g](https://doi.org/10.1021/ma402566g)
- [36] Liang X, Ito M, Nakajima K. Reinforcement mechanism of carbon black-filled rubber nanocomposite as revealed by atomic force microscopy nanomechanics. *Polymers (Basel)*. 2021;13(22):3922. doi: [10.3390/polym13223922](https://doi.org/10.3390/polym13223922)
- [37] Dechnarong N, Kamitani K, Cheng CH, et al. In situ synchrotron radiation x-ray scattering investigation of a microphase-separated structure of thermoplastic elastomers under uniaxial and equi-biaxial deformation modes. *Macromolecules*. 2020;53(20):8901–8909. doi: [10.1021/acs.macromol.0c00962](https://doi.org/10.1021/acs.macromol.0c00962)
- [38] Tomita S, Wataoka I, Igarashi N, et al. Strain-induced deformation of glassy spherical microdomains in elastomeric triblock copolymer films: time-resolved 2d-saxs measurements under stretched state. *Macromolecules*. 2017;50(8):3404–3410. doi: [10.1021/acs.macromol.6b02797](https://doi.org/10.1021/acs.macromol.6b02797)